Brain Pathology ISSN 1015-6305

RESEARCH ARTICLE

Stimulation of retrotrapezoid nucleus Phox2b-expressing neurons rescues breathing dysfunction in an experimental Parkinson's disease rat model

Silvio A. Fernandes-Junior[1,2]; Luiz M. Oliveira[1]; Catherine M. Czeisler[2]; Xiaokui Mo[3]; Sashwati Roy[4]; Arpad Somogyi[5]; Liewn Zhang[5]; Thiago S. Moreira[6]; José J. Otero[2*]; Ana C. Takakura[1,*]

[1] Department of Pharmacology, Instituto de Ciencias Biomedicas, Universidade de Sao Paulo (USP), São Paulo, Brazil.
[2] Department of Pathology, School of Medicine, The Ohio State University (OSU), Columbus, OH.
[3] Department of Biostatistics and Bioinformatics, The Ohio State University (OSU), Columbus, OH.
[4] Departments of Surgery and Molecular and Cellular Biochemistry, The Ohio State University (OSU), Columbus, OH.
[5] Mass Spectrometry and Proteomics Facility, The Ohio State University (OSU), Columbus, OH.
[6] Department of Physiology and Biophysics, Instituto de Ciencias Biomedicas, Universidade de Sao Paulo (USP), São Paulo, Brazil.

Keywords
Parkinson's disease, photo-stimulation, proteomics, respiration, retrotrapezoid nucleus.

Corresponding author:
Ana C. Takakura, PhD, Department of Pharmacology, Instituto de Ciencias Biomedicas, Universidade de Sao Paulo, 1524, Prof. Lineu Prestes Avenue, 05508-000 São Paulo, SP, Brazil (E-mail: *takakura@icb.usp.br*)
José Javier Otero, MD, PhD, Department of Pathology, The Ohio State University College of Medicine, 4166 Graves Hall, 333 W 10th Avenue, Columbus, OH 43210 (E-mail: *jose.otero@osumc.edu*)

Received 16 January 2020
Accepted 11 May 2020
Published Online Article
Accepted 4 June 2020

*José J. Otero and Ana C. Takakura are equivalent corresponding authors.

doi:10.1111/bpa.12868

Abstract

Emerging evidence from multiple studies indicates that Parkinson's disease (PD) patients suffer from a spectrum of autonomic and respiratory motor deficiencies in addition to the classical motor symptoms attributed to substantia nigra degeneration of dopaminergic neurons. Animal models of PD show a decrease in the resting respiratory rate as well as a decrease in the number of *Phox2b*-expressing retrotrapezoid nucleus (RTN) neurons. The aim of this study was to determine the extent to which substantia nigra pars compact (SNc) degeneration induced RTN biomolecular changes and to identify the extent to which RTN pharmacological or optogenetic stimulations rescue respiratory function following PD-induction. SNc degeneration was achieved in adult male Wistar rats by bilateral striatal 6-hydroxydopamine injection. For proteomic analysis, laser capture microdissection and pressure catapulting were used to isolate the RTN for subsequent comparative proteomic analysis and Ingenuity Pathway Analysis (IPA). The respiratory parameters were evaluated by whole-body plethysmography and electromyographic analysis of respiratory muscles. The results confirmed reduction in the number of dopaminergic neurons of SNc and respiratory rate in the PD-animals. Our proteomic data suggested extensive RTN remodeling, and that pharmacological or optogenetic stimulations of the diseased RTN neurons promoted rescued the respiratory deficiency. Our data indicate that despite neuroanatomical and biomolecular RTN pathologies, that RTN-directed interventions can rescue respiratory control dysfunction.

INTRODUCTION

The clinical spectrum of Parkinson's disease (PD) manifestations has continued to evolve with improvements in patient management and therapies. James Parkinson's original description of patients showing specific types of tremor and rigiditiesis has entrenched a concept of PD focused on movement impairments (12, 50). However, most neurologists now have begun to appreciate that patients presenting with these classical motor symptoms also suffer from a plethora of other symptoms affecting different brain regions. For instance, autonomic and somatic nervous system dysfunctions affect 70%–80% of Parkinson's patients (58, 71). These symptoms range from breathing abnormalities during sleep or awake vigilance states, bowel and bladder dysfunction, and cardiovascular dysregulation such as orthostatic hypotension. The mechanistic underpinnings of these pathologies remain poorly understood. For instance, it is not clear that dysfunction of non-nigral neural circuits that occurs in PD is caused by pathological alpha-synuclein accumulation within the non-nigral neural circuit, or if this is caused by other known neurodegenerative processes such as trans-synaptic circuit degeneration. The recent finding from our group showing projections from substantia nigra pars compacta (SNc) to the retrotrapezoid nucleus (RTN) in the rodent via periaqueductal gray substance (PAG) underscores the

New Findings

What is the central question of this study?

- Are there biomolecular changes in RTN region of experimental model of PD? Can the ventilatory deficit of animals submitted to the experimental model of PD be reversed with the stimulation of the Phox2b neurons of the RTN?

What is the main finding and its importance?

- Respiratory problems may be responsible for much of the mortality and morbidity associated with PD, but data related to central respiratory changes are still lacking in the literature. In the present study we confirmed reduction in the number of neurons in RTN region and deficit in breathing in a model of PD.
- The present data also provided the first evidence of biomolecular changes in the RTN region and stimulation of the remaining RTN Phox2b neurons restores the ventilatory deficits in a model of PD.

possibility that SNc degeneration could induce RTN neurodegeneration through trans-synaptic mechanisms (38).

An advantage of the 6-hydroxydopamine (6-OHDA) injection model for PD is that it incisively tests 6-OHDA toxicity in SNc without confounding factors of alpha-synuclein accumulations. 6-OHDA injection into the rat striatum (caudate-putamen region: CPu) induces baseline respiratory changes starting 40 days post injury (26, 49, 67). A reduction of medullary neurons occurring 30 days post injury was noted in RTN and the nucleus of the solitary tract (NTS), which was correlated with ventilatory changes (26). In this study, we test the hypothesis that SNc degeneration in and of itself induces RTN biomolecular changes and demonstrate that exogenous RTN activation rescues PD-associate autonomic pathophysiologies. To test this hypothesis, we performed comparative proteomic analysis on laser capture microdissection and pressure catapulting of RTN and neuronal stimulation through both pharmacological and optogenetic modalities of remaining RTN neurons while recording breathing in conscious and anesthetized animals.

MATERIALS AND METHODS

Ethical aproval

All experimental and surgical procedures were conformed to the guidelines of the National Institutes of Health and were approved by the Institutional Animal Care and Use Committee at the University of São Paulo (CEUA # 104/23/03) and Institutional Animal Care and Use Committee of The Ohio State University (IACUC #2012A00000162-R1).

Animals

The experiments were performed in 31 male Wistar rats weighing 250–300 g. The animals were distributed into three different groups: biomolecular analysis (6-OHDA, n = 4; vehicle, n = 4), pharmacological stimulation (6-OHDA, n = 4; vehicle, n = 4) and optogenetic stimulation (6-OHDA, n = 8; vehicle, n = 7). The animals had free access to water and food and were housed in a temperature-controlled chamber at 24°C with a 12:12 h light/dark cycle.

Experimental model

The induction of the PD model was performed by bilateral injection of 6-OHDA (6-OHDA hydrochloride, H4381, Sigma, Saint Louis, MO, USA, 24 µg/µL) or vehicle (1 µg ascorbic acid in 1 µL of saline) in the CPu, while the rats were anesthetized intraperitoneally (i.p.) with ketamine (100 mg/kg) and xylazine (7 mg/kg) (Davol, São Paulo, SP, Brazil), as previously described (24, 26, 67). The rats were placed in a stereotaxic frame (model 1760, David Kopf Instruments), and 6-OHDA (0.5 µL/injection) was injected into the CPu at two locations on each side of the brain, at the following coordinates: (i) AP: 0 mm rostral to Bregma, ±2.7 mm lateral to midline, 4.5 mm below the skull surface; and (ii) 0.5 mm rostral to Bregma, ±3.2 mm lateral to midline, 4.5 mm below the skull surface. The injections were made using pipettes with an external tip coupled to a Hamilton syringe (10 µL). The 6-OHDA neurotoxin when injected in mammals such as mice, rats or monkeys, is collected up by dopaminergic neurons via the dopamine and norepinephrine reuptake transporters. In the case of striatum, the neurotoxin is retrogradely transported and selectively kills dopaminergic neurons of the substantia nigra pars compacta (33).

Biomolecular analysis in the RTN

For biomolecular analysis, 60 days after induction of the PD model, we used microdissection and suction with laser capture microdissection (LCM) coupled to an inverted microscope (PalmRobo 4.5 Technologies, Carl Zeiss, MicroImaging GmbH, Munchen, Germany) (56). We obtained tissues from the RTN region by cryogenics at controlled temperature (Cryostate, Leica/CM 1800). We used 1 in 10 series of 12 µm brain sections per animal, totaling a distance of 120 µm between the cuts. We considered the eight most rostral cuts to the caudal portion of the facial nucleus (Bregma −11.60 mm). Thus, the analyzed sections correspond to the Bregma interval between −10.76 and −11.60 mm, covering a total range of 840 µm among the Bregmas. The slices were then mounted on special slides of polyethylene naphthalate membrane (PEN-Membrane Slide 1.0 mm, Carl Zeiss®) that allows cutting and obtaining biological tissues under controlled microscopy (56). The laser cut of each section was sucked up to a micro Eppendorf coupled at the base of the system. We then submerged the tissues in a specific enzyme digestion solution (RapiGest™ SF surfactant, Water Corporation, Milford, MA, USA) and stored in −80°C freezer.

We performed mass spectrometric analyses from samples pooled from eight RTN cuts per animal (59). The tissues were analyzed sequentially by liquid chromatography-mass spectrometry (LC/MS) using an Orbitrap Mass Spectrometer. We thawed samples and sonicated them at low power for a total time of 60 s, 3 s on followed by 3 s off. The samples were boiled at 100°C for 5 minutes and cooled to room temperature. An aliquot was then removed for protein concentration determination. Samples were digested overnight with 1:30 trypsin:protein at 37°C. The digestion was stopped through the addition of 0.5% trifluoroacetic acid (TFA). The solution was centrifuged at 13.000 for 5 minutes and the supernatant removed and dried in a speedivac. Samples were stored at −80°C until analysis. Before analysis, samples were resuspended in 50 mM acetic acid. Liquid chromatography-nanospray tandem mass spectrometry (LC/MS/MS) of protein identification was performed on a Thermo Scientific orbitrap Fusion mass spectrometer equipped with an EASY-Spray™ Sources operated in positive ion mode. Data analysis were performed using Mascot 2.6.0. Data were filtered to enable only proteins for which two unique peptides to be considered, along with high confidence identifications (1% FDR). Search results were compiled in Scaffold, using a 1% FDR for proteins and enabling comparison between samples (vehicle × 6-OHDA group). For the final interpretation of the data we used a biostatistical analysis tool of the gene expression and proteomics, based on the Ingenuity Knowledge Base (IPA® - *Ingenuity Pathway Analysis*) (32).

Selective stimulation of Phox2b expressing neurons in RTN

Stereotaxic surgery was used for pharmacological stimulation or to target opsin gene expression to genetically define and spatially restricted neuronal populations in the brain and used to place a light delivery device to target the transduced cells (Phox2b neurons in RTN region). For pharmacological stimulation, fifty days after the vehicle or 6-OHDA injections in CPu, eight animals underwent surgical procedures for the implantation of bilateral guide cannulas (15 mm length) in the RTN region. Using the lambda as reference, a trepanation of the skull bone was made by opening a 1.5 mm diameter hole. The coordinates used were: (i) 1.8 mm lateral to midline; (ii) 2.7 mm caudal to lambda and (iii) 5.5 mm ventral to dura mater. The cannulae were fixed to the heads of the rats with screws and acrylic resin. Ten days later, the N-methyl D-Aspartateglutamatergic agonist (NMDA, 5 pmol/50 nL, Sigma Chemicals Co.) or saline (50 nL) was injected into the RTN of unanesthetized rats by an injection needle (18.5 mm in length). The same animal was tested twice (one per side) to increase the chance of targeting RTN.

For the optogenetic experiments, the photo-stimulation was performed in the same animals on awake and anesthetized conditions. Thirty days after the injection of the 6-OHDA or vehicle in the CPu, the surgical procedures for the injection of the viral construct and fixation of the guidewire were performed. Here, we used the viral promoter (PRSx8) to identify the Phox2b neurons associated with the rhodopsin 2 channel (ChR2) and a fluorescent component for later histological identification. The lentiviral vector was prepared using a previously described construct (pLenti-PRSx8-hChR2(H134R)-eYFP-WPRE; abbreviated PRSx8-ChR2-eYFP) which features an enhanced version of the photoactivatable cationic channel ChR2 (H13R) fused to the fluorescent protein eYFP (1, 44). Transgene expression was under the control of a synthetic Phox2-selective promoter (PRSx8) (2-4,7,15,17,31,42). Briefly, pSPAX2 and VSV-g were used as the packaging plasmids and co-transfected with the PRSx8-ChR2-eYFP through the calcium phosphate precipitation method. Lentiviral supernatants were collected 24 and 48 h after transfection, followed by concentration by ultracentrifugation at 23.000 rpm during 90 minutes at 4°C in a swinging bucket rotor (SW32Ti, Beckman Coulter, Brea, CA, USA). After centrifugation, medium was discarded and pellet was resuspended in 25 µL of Hank's Balanced Salt Solution (Life Technologies, CA, USA), aliquoted and stored in a −80°C freezer. We assessed virus titer by ELISA kit QuickTiterTMLentivirus Titer kit (Cell Biolabs, Inc, USA). The viral vectors were injected through a glass needle (1.2 mm internal diameter with a 25 µm opening diameter) into the RTN region by pressure (Picospritzer III, Parker Hannifin, Cleveland, OH, USA, 20 Psi, for 8 to 12 ms, 200 nL) at points: (i) 1.8 mm lateral to the midline; (ii) 2.4 and 2.6 mm caudal to lambda; and (iii) 8.4 mm ventral to the dura mater. A guide cannula was also implanted for opto stimulation: (i) 1.8 mm lateral to the midline; (ii) 2.5 mm caudal to the lambda; and (iii) 8.0 mm ventral to the dura mater. Thirty days later, the experiments with awake animals were performed. An optical fiber (200 µm in diameter—ThorLabs, Newton, NJ, USA) was inserted through the cannula guide to selective activate Phox2b neurons and the ventilatory parameters were recorded by whole-body plethysmography (63). The activation of this fiber allows the emission of blue light laser (470–473 nm- 10–30 mW- 1.9–3.9 mA- 5–20 Hz- 10 s–1 minute, CrystaLaser Mode BC-473-050-M; Reno, NV) (1, 54), by the power amplifier (M470F3, ThorLabs) and adjusted by the optical controller (DC2200 High-Power LED controller, ThorLabs, USA) and activation of the Phox2b neurons.

In the next day, the same animals were anesthetized, and the photo-stimulation was again performed, and the breathing parameters were recorded by electromyography of respiratory muscles.

Measurements of respiratory parameters

Conscious rats

Breathing analysis in conscious rats was performed 60 days after vehicle or 6-OHDA injections by whole-body plethysmography method, as previously described (EMKA Technologies) (26). Briefly, freely moving rats were kept in a 5-L plethysmography chamber with room air for

45–60 minutes before the ventilatory parameters were recorded. The plethysmography chamber was continuously operated at a set temperature with humidified inflow gas (23–25°C ambient room temperature, 60%–70% relative humidity, ±0.5°C, ±5% relative humidity). The chamber was also continuously flushed at 1.5 L/min, as regulated by computer-driven mass flow controllers for oxygen (O_2), nitrogen (N_2), and carbon dioxide gas (CO_2) (Alicat Scientific, Inc., Tucson, AZ, USA). The flow controllers were adjusted to 21% O_2 balanced with N_2 in normoxia, 7% CO_2, 21% O_2 and 72% N_2 in hypercapnia and to 8% O_2, and 92% N_2 in hypoxia. In maximal chemoreflex stimulation (MCS) protocol, the animals were submitted to concentration of 8% O_2 and 7% CO_2 balanced with N_2. The hypercapnia, hypoxia and MCS protocols were performed for 10 minutes each and analysis were performed every second. Rectal temperature was used as a core body temperature index and was measured before and at the end of every experiment. The calibration of volume was obtained by waveforms generated during each experiment by injecting the animal chamber with 20 mL of dry air, as calculated using Spike software version 7.3 (Cambridge Electronics). The breathing parameters measured by the plethysmography system were tidal volume (V_T, mL/kg of body weight; area under the curve during the inspiratory period) and respiratory frequency (f_R, breaths/min). Ventilation (V_E, mL/min/kg of body weight) was calculated as the product of f_R and V_T. The measurements were performed 1 day before and 60 days after vehicle or 6-OHDA injection into the CPu.

For pharmacological or optogenetic stimulations, the animals were placed in the other kind of plethysmography chamber model for recording respiratory variables, adapted for external stimulation and simultaneous reading (LabChart Reader v8.1.2-2016; ADInstruments). The respiratory recordings were performed at rest and during pharmacological or optogenetic stimulations. For pharmacological stimulation, after the baseline recording, saline or NMDA was injected in control and 6-OHDA- animals in the RTN region and the respiratory parameters were analyzed during 60 s after stimulation. For optogenetic stimulation, after baseline recording, a fiber optic cable was connected to a fixed guide cannula previously implanted in the RTN region and the photo-stimulation was performed by blue light laser in both groups and the respiratory parameters were analyzed 20 s to 1 minute after laser activation. The signals were amplified, filtered, recorded by the LabChart software and then, analyzed by the reading software (LabChart Reader v8.1.2-2016; ADInstruments). The following settings were used: 470 nm, 20 mW, 3.9 mA, with alternating pulses of 20 s, 10–20 Hz, 10 ms on/off.

Anesthetized rats

The same group of animals that received the photo-stimulation of RTN described previously were in the next day anesthetized, the photo-stimulation was through the ventral surface and the ventilatory parameters were analyzed by recording the electrical activity of the respiratory muscles: diaphragm and abdominal, as previously described (48,60,61).

Briefly, the animals were anesthetized with isoflurane (5%) in 100% oxygen. Subsequently, they were tracheostomized with a metal cannula and coupled to mechanical ventilation maintained in 2% isoflurane diluted in 100% oxygen. The respiratory rate was adjusted to 60–80 cycles/s, 1–1.2 mL/100 g and a positive end-expiratory pressure (PEEP) of 1 cmH_2O during the surgical and experimental procedures and the temperature was maintained at 37°C using a mattress with internal resistance for heating. The animals were bilaterally vagotomized and received the cannulation of the femoral artery and vein for recording pulsatile arterial pressure (PAP) and administration of anesthetics, respectively. Silver electrodes were positioned in the diaphragm and abdominal muscles to record the electromyographic inspiratory and active expiratory activities, respectively. At the end of the surgical procedures, the inhaled anesthetic isoflurane was replaced by the endovenous urethane anesthetic (1.2–1.4 g/kg), keeping the animals ventilated with 100% oxygen. All signals were amplified at 20 K, filtered from 100 to 3000 Hz and acquired through an 8-channel digital analog converter (CED 1401, Cambridge Electronic Design, UK). The signal was copied to a Spike 2 software version 6.16 data acquisition system (CED, Cambridge Electronic Design, UK). Noise was subtracted and resting muscle activities (frequency and amplitude) were considered at the time immediately before Phox2b RTN optogenetic stimulation. The activities were normalized to 100%, and the delta percentage was used to compare the changes produced during 10 s of photo-stimulation (6, 8, 42).

Immunohistochemistry, image acquisition and cell counting

At the end of the experiments, the animals were deeply anesthetized with sodium thiopental (60 mg/kg, i.p.) and perfused through the ascending aorta with 350 mL of heparinized saline (pH 7.4) followed by 500 mL of 4% phosphate-buffered paraformaldehyde (PFA, pH 7.4). Brains were removed and fixed in PFA for 1–2 days at 4°C. Series of coronal sections (40 or 12 μm) from the brain were cut using a cryostat (Leica/CM 1800) and stored in cryoprotectant solution at −20°C (20% glycerol plus 30% ethylene glycol in 50 mL phosphate buffer, pH 7.4) for up 2 weeks until histological processing (57). All histological procedures were performed with free-floating sections. No labeling was observed when the primary antibodies were omitted. Sections were rinsed, blocked and stained via the immunoperoxidase method with antibody specific for detection of tyrosine hydroxylase (TH^+) (Chemicon, Temecula, CA, USA) and Phox2b$^+$ (DAKO EnVision™+ System, HRP) as previously described (26) and via the fluorescent method for detection of green fluorescent protein (GFP^+). The sections were mounted on gelatinized slides in a rostrocaudal sequence and subsequently dehydrated in alcohol and covered with DPX Mountant (Aldrich, Milwaukee, WI, USA).

For neuroanatomical analysis, in a rostral-caudal aspect of the SNc, we measured every sixth 40 µm brain section, in a total distance of 240 µm between each pair of sections analyzed. In a medial-lateral aspect, the whole SNc was measured in every section analyzed. In the designed-based approach (stereology), quantification can be performed in thicker sections (20–100 microns). The reason we use 40 microns is the fact that the *z*-stack can help in analyzing the number of neurons and the penetration of the antibody is optimized at that thickness (29, 62, 68). In this protocol, a multifunction microscope (NIKON Eclipse E-1000) coupled to a digital camera (NIKON DXM-1200) was used to image sections and to perform subsequent analysis (52, 57) and ImageJ (version 1.41; National Institutes of Health, Bethesda, MD) and Canvas software (ACD Systems, Victoria, Canada, v. 9.0) were used for cell counting and line drawings, respectively.

For biomolecular analysis, we used a specific histological procedure for neuronal quantification and subsequent protein extraction. Every 10th 12 µm brain section was used, in a total distance of 120 µm between each pair of sections analyzed. The cell counting was performed by stereological quantifications using the simultaneous image fragmentation system. We used the optical shredder sampling (Axio microscope, Carl Zeiss, Imager.M2, HAL 100), in 10× (low magnification) lenses to delineate the analysis area and 40× (high magnification) to add the counting markers. For the final quantification, Stereo Investigator Neurolucida software (version 2017; MBF Bioscience, Optical Fractionator 3D, Williston, Vermont, USA) was used (29, 40, 62, 68).

For both protocols, the sections were analyzed bilaterally, and the numbers reported in the results section correspond exactly to the total counts of each section in a series. Briefly, to align sections around the SNc level, five sections were considered at the end of the medial geniculate nucleus and assigned the level 6.04 mm caudal to bregma (interval between −5.34 and −6.30 mm). To align sections around the RTN, three sections with the most caudal section that contained an identifiable cluster of facial motor neurons were identified in each brain and assigned the level of 11.6 mm caudal to bregma (interval between −11.12 and −11.60 mm).

For the machine learning-based image analysis workflow (Figure 1), we captured microscopic images 10× images of the anti-Phox2b immunostained section of rat medulla. Representative images from at least three animals per condition were captured using a Carl Zeiss Imager M.1 microscope and Stereoinvestigator™ Software under 10× magnification (NA = 0.25), and subsequently saved as .tif files.

These files were opened in photoshop, and the RTN was selected, copied, and saved as a .tif file. Capturing the images at low magnification was critical to preserve the neuroanatomical boundaries of the RTN, as well as to capture similar images as those used for the unbiased manual quantification performed. The .tif files were then imported into Rstudio using the EBImage package (51). These .tif images were RGB format, and then, converted to Grayscale in Rstudio and inverted. We then generated a custom script that included local adaptive thresholding, and morphological operations using available in EBImage. The binary images were used to create segmented masks, which were then overlaid on the grayscale image. All thresholding parameters were optimized on control images and applied to the all images. Imaging features were extracted from each segmented object. The computer features function call in EBImage extracted the intensity features, including mean (mean pixel intensity), q001 (1st percentile intensity), q005 (5th percentile intensity), q05 (50th percentile intensity), q095 (95th percentile intensity), q99 (99th percentile intensity), shape features, including major axis (elliptical fit of major axis), eccentricity (eccentricity = 0 for circle and eccentricity = 1 for straight line) and theta (object angle, in radians), and the Haralick texture features (28), including asm (angular second moment, a measure of homogeneity of the object), con (contrast), cor (correlation), var (sum of squares variance), idm (inverse difference moment), sav (sum average), sva (sum variance), sen (sum entropy), ent (entropy, demonstrating the randomness of all of the pixels), dva (difference variance), the den (difference entropy), f12 and f13. These features were extracted and saved into a rectangular data table, which was then reimported into R and class labels were generated.

In the machine learning tests, we utilized the following R packages: caret (34), random forest (37), Boruta (35). To prevent class imbalance problems, we generated a pooled dataset containing all of the experimental objects (which were fewer than the quantity of segmented objects in control, a finding in concordance with our stereological quantification). The pooled objects from both the control and experimental (which represent Phox2b-immunoeactive nuclei or nuclear fragments detected in the auto-threshold step) were then split into two pools: 70% were randomly selected for training, and 30% for testing. We then constructed a random forest with 500 trees and passed the training data to the Boruta algorithm to identify imaging features that were deemed unimportant. The confirmed features were then selected and used to train a new random forest on the training data (composed of 500 trees). After training, we tested the efficiency of the algorithm on the test data. We used the confusion Matrix function call in the Caret package for accuracy estimates. The graphs were plotted using the ggplot2 library (69).

Statistical analysis

Statistical analysis was performed using the programs Sigma Stat 3.0 (Jandel Corporation, Point Richmond, CA) and R (R Core Team, 2017). Linear models were generated using base R statistical package. All data are presented as the mean ± standard deviation of the mean (SDM). One-way repeated-measures ANOVA was followed by Bonferroni (functional analysis) or Tukey (neuroanatomical analysis) post-tests, as indicated. In mass spectrometry analysis, label free relative quantification was accomplished by the spectral count approach (18, 39) in which the number of MS/MS spectra identified from the same protein is used to represent relative protein abundance. Significance

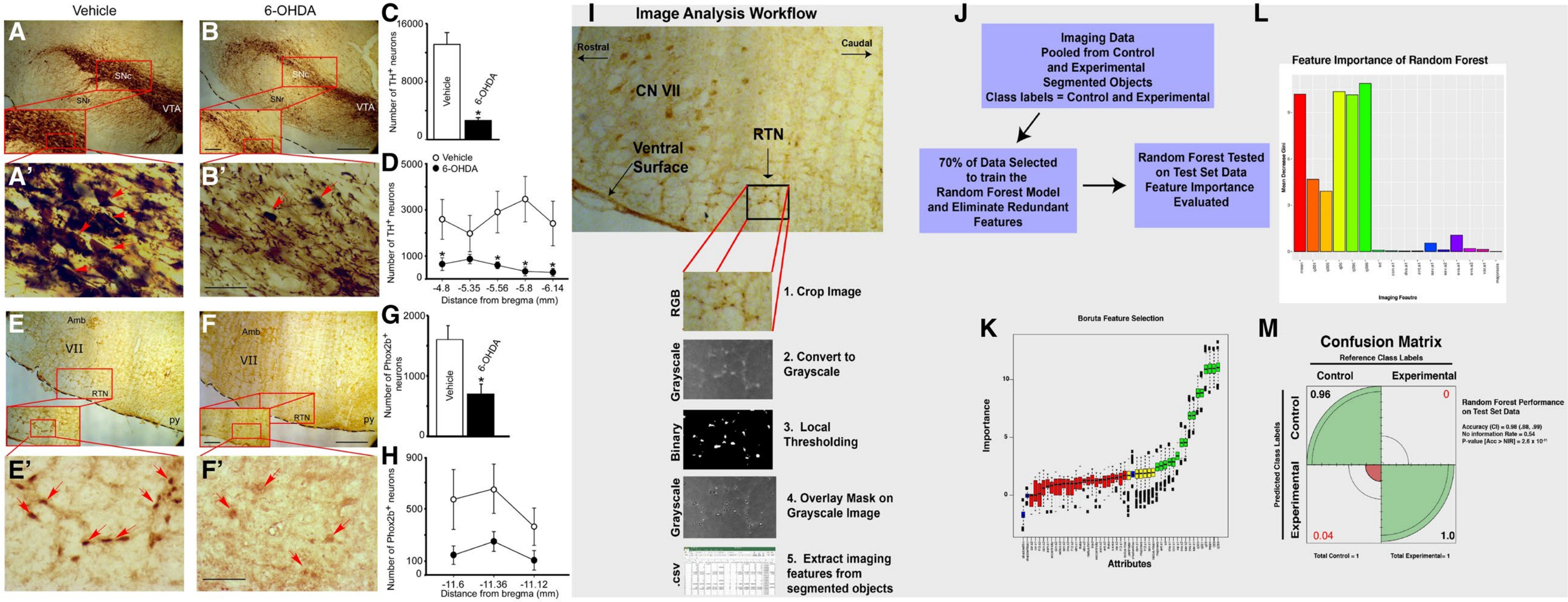

Figure 1. *SNc and RTN after induction of the experimental model of PD.* Photomicrographs of SNc of animals that received bilateral injection of vehicle (**A**) or 6-OHDA (24 µg/µL) (**B**) in the CPu and were sacrificed 60 days after injection (Bregma −5.82 mm). Total number (**C**) or the distribution by bregma (**D**) of TH^+ neurons in SNc. Photomicrographs of RTN of animals that received bilateral injection of vehicle (**E**) or 6-OHDA (24 µg/µL) (F) in the CPu and were sacrificed 60 days after injection (Bregma −11.6 mm). Total number (**G**) or the distribution by bregma (**H**) of $Phox2b^+$ neurons in RTN. A′, B′, E′ and F′ represent a higher magnification of the red rectangles in A, B, E and F, respectively. The arrows represent examples of TH^+ and $Phox2b^+$neurons. **I.** Image analysis workflow illustrated in a vertical step-wise process. For detailed discussion, see Methods and supplemental material. In (**J**) general workflow of the machine learning approach. The data were controlled for class imbalance by undersampling the control data, and then, pooled into one data table. About 70% was extracted for training, 30% extracted for testing. In the training data step, we performed feature selection using the Baruta algorithm (**K**). Feature importance is plotted on the *Y*-axis. Box plots represent data from the various runs of the Boruta algorithm. Blue boxes demonstrate the minimum, median, and maximum shadow feature performance. Features in green (confirmed importance), yellow (indeterminant importance) and red (rejected by the Boruta algorithm). Random forest importance trained on the training data set was interrogated for feature importance (**L**). Results of the confusion matrix plotted using the fourfold plot function in R (**M**), which plots a 2 by 2 table shown as a quarter circle, so that the area of the semicircle in the quadrant is proportional to the frequency. Confidence intervals are highlighted by the rings within the semicircle. One-way ANOVA followed by Tukey's post hoc test was used. * $P < 0.05$ in relation to the vehicle group. Data obtained from four animals (TH^+) or 3 animals ($Phox2b^+$) per group. Data displayed as mean ± SD. Abbreviations: Acc = accuracy; Amb = nucleus ambiguous; CN VII = seventh cranial nerve; NIR = no information rate; py = pyramidal tract; SNc = substantianigra pars compact; SNr = substantianigra pars reticulated; VTA = ventral tegmental area; VII = motor nucleus of the facial nerve. Scale in B and F = 200 µm (applies to A–E); zoom in B and F = 100 µm (zoom applies in A and E) and B′–F′ = 50 µm (applies to A′–E′).

analysis of relative protein abundance was determined by analysis of the spectral count data using the edgeR bioconductor package (54). Peptide spectral counts were modeled as an over dispersed Poisson/negative binomial distribution in which an empirical Bayes procedure was used to moderate over dispersion across each protein. A Benjamini–Hochberg multi-test correction (α = 0.05) was applied to final p-values to control for false discoveries (10). A statistical threshold of P < 0.05 with fold-change (FC) ≥2 was considered as significant for identification of differentially expressed genes. The level of significance considered in all tests was 5%.

RESULT

Biomolecular changes observed in RTN following 6-OHDA-induced SNc toxicity

Prior studies have demonstrated that bilateral injections in CPu reduced TH^+ SNc neurons, which we use as an experimental paradigm for PD, reduces Phox2b neurons in RTN (26). Phox2b+ neurons in the RTN regulate central chemoreception (45,64,65). Therefore, we set out to determine the extent to which SNc degeneration induced biomolecular changes in the RTN. SNc degeneration was induced by stereotaxical administration of 6-OHDA into the CPu (see methods)46. To quantify induced neurodegeneration, we counted neuronal number by stereologically quantifying SNc TH^+ neurons and RTN $Phox2b^+$ neurons. Evaluation 60 days post-6-OHDA injection into the CPu showed a reductionof 79% in SNc TH^+ immunoreactive neurons (6-OHDA:2638 ± 378; vs. vehicle:13129 ± 1619 neurons; P < 0.001) (Figure 1A–D) and 56% in the number of Phox2b-expressing neurons in RTN region (6-OHDA:704 ± 159; vs. vehicle, 1596 ± 235 neurons; P < 0.05) (Figure 1E–H). We confirmed that bilateral 6-OHDA injection promotes degeneration of catecholaminergic neurons in the SNc as well as $Phox2b^+$ neurons in the RTN.

We noted during our unbiased stereological quantification that the morphology of the Phox2b immunoreactive cells in the 6-OHDA-injected animals was different than the control cells (compare the cells in the red arrows in Figure 1, panels E′ and F′). To confirm this, we generated an objective, automated image analysis workflow to segment the Phox2b immunoreactive nuclei. This workflow, illustrated in Figure 1I, we developed using control imaging data from the same slides utilized for unbiased stereological quantification, and resulted in successful segmentation of Phox2b-immunoreactive nuclei and nuclear fragments (see methods for details, as well as code in Supporting Information). We tested the hypothesis that automatically segmented nuclei from control or 6-OHDA (designated experimental in this workflow) were different by training a random forest algorithm to fit data into the class labels "control" or "experimental." Successful class labeling by such an algorithm would indicate that clear differences exist in the features of segmented nuclei (see machine learning workflow in Figure 1J). After separating 70% of the data for training, we removed unnecessary features by implementing the Boruta algorithm, which shuffles randomly each feature into a shadow feature, and compares the performance of the actual feature to the shadow feature; features that perform just as well as in classification as their shadow features were rejected. We then utilized the confirmed features to train a random forest to label segmented nuclei as having been derived from control or experimental images. The feature importance of the algorithm is graphed in Figure 1L. Note that this model utilized principally features of intensity in its classification. This model was then trained on the test data to determine algorithm accuracy, and the confusion matrix of the data are shown in Figure 1M. Note that the accuracy of class labeling was very high (~98%), a finding that was statistically significant.

In summary, using unbiased image segmentation and supervised machine learning, we were able to train a random forest to correctly determine the experimental condition of objects segmented from images of Phox2b-immunostained sections. We conclude that 6-OHDA treated animals induce both (i) a reduction in the number of Phox2b-immunoreactie RTN neurons; and (ii) a change in Phox2b morphology within these neurons, principally characterized by reduction in staining intensity.

Having validated significant reduction in the number of neurons in our models, we next set out to test the extent to which respiratory function was impaired by SNc degeneration. Functional analyses, performed 60 days post-injection, included plethysmographic recordings of breathing in basal room air conditions and during three chemosensory challenges: (i) hypoxia; (ii) hypercapnia; and (iii) hypoxia with hypercapnia (maximal chemosensory stimulation, MCS). Respiratory parameters every minute during 10 minutes of each condition were measured as well as extraction of the arithmetic mean over the 10 minutes interval (Figure 2). We noted a reduction in resting and hypercapnia ventilatory responses when compared to basal condition (f_R, V_T and V_E) in 6-OHDA treated animals compared to control (Figure 2D–F). 6-OHDA treatment also showed reduced values the hypoxia and MCS respiratory responses (Figure 2D–F). In summary, significant ventilation dysfunction was noted in the PD group.

In order to obtain further insights into PD-induced respiratory pathophysiology, we utilized a machine learning approach to interrogate our data (53). To achieve this, we first fit our data to a multivariate linear regression model where respiratory parameters f_R, V_T, or V_E were modeled as response variables, and the gas challenges (hypercapnia, hypoxia, or MCS) and PD-status, modeled as factors, were predictor variables with interactions. The model's details are shown in Table 1. The adjusted R-squared of each model was over 0.95, indicating that f_R, V_T or V_E were highly dependent on these factors. These data indicate that hypercapnia, hypoxia and MCS all increase f_R, V_T and V_E, whereas positive PD-status decreases significantly each respiratory parameter evaluated. However, in f_R, PD-status does not show statistically significant interaction with any of the gas challenges (note that the p-value for interaction of PD to

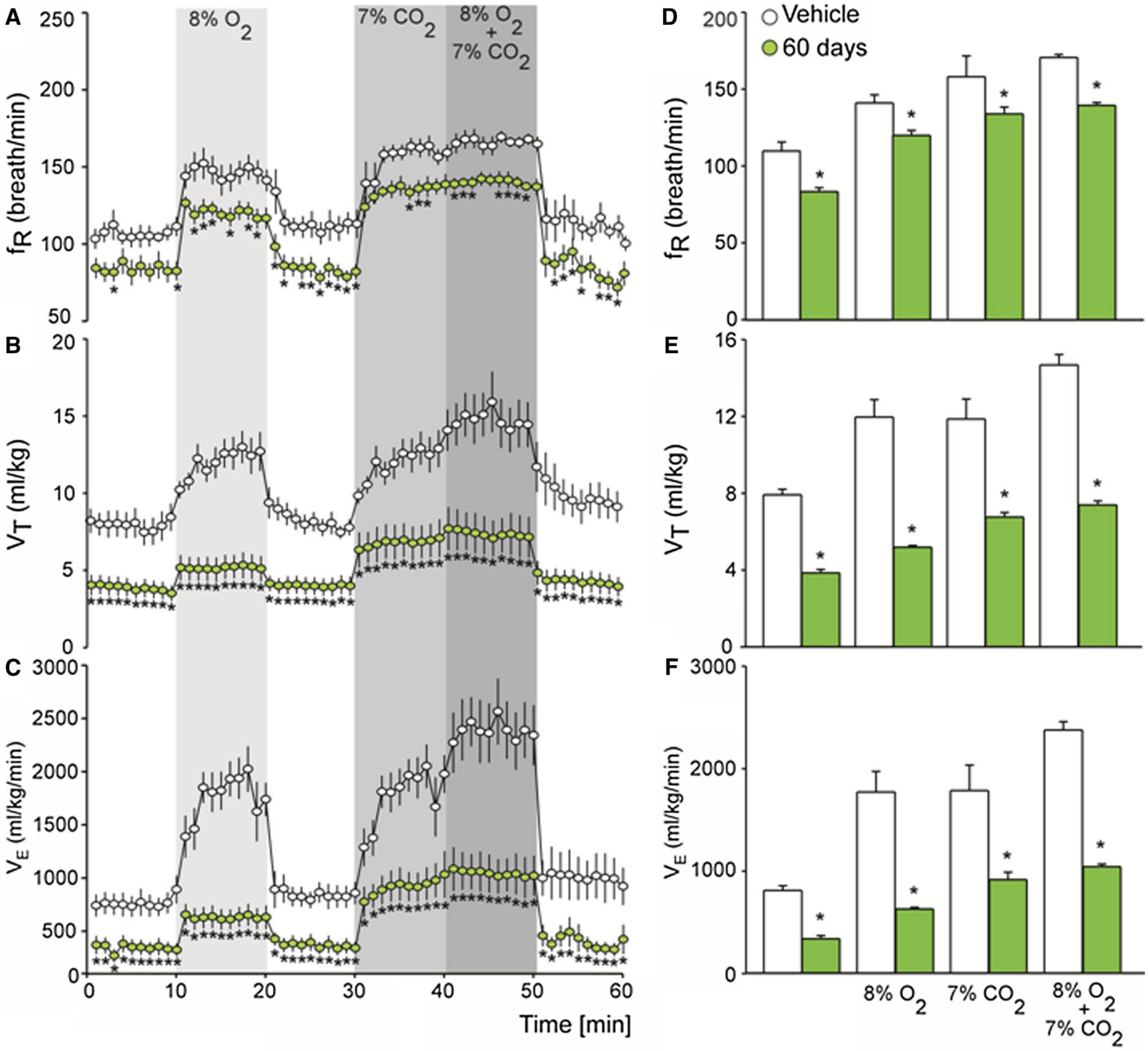

Figure 2. *Ventilatory changes after induction of the experimental model of PD.* Minute by minute or meanchanges in f_R (**A** and **D**), V_T (**B** and **E**) and V_E (**C** and **F**) during resting, hypoxia, hypercapnia or maximal chemoreflex stimulation (MCS) produced 60 days after bilateral injection of vehicle or 6-OHDA (24 µg/µL). Two-way ANOVA with repeated measures and post hoc of Bonferroni tests, (minute by minute changes) and One-way ANOVA with Tukey's post hoc test (mean changes). *P < 0.05 in relation to the vehicle group. Data displayed as mean ± SD.

the gas challenges are all over 0.1 in the f_R analysis), indicating that PD-status does not alter chemosensory increase in respiratory rate. In contrast, positive PD-status showed significant interaction with hypoxia and MCS, indicating that PD-status altered some components of the hypoxia-induced chemosensory response. V_E, which represents the product of f_R and V_T, showed significant interaction of PD with all of the gas challenges. This indicates that in the PD-positive animals, the relationships between f_R and V_T were altered. We conclude that the PD-positive status shows significant changes in hypercapnic and hypoxic chemosensory responses, in addition to showing repression of baseline respiration (Figure 2A–C).

6-OHDA treatment induces biomolecular changes in the RTN

We evaluated the extent to which the RTN showed biomolecular changes in addition to the decreases in RTN neuronal number. Proteomics have been applied in sophisticated brain analysis in order to map and facilitate the understanding of neurodegenerative processes (32, 55). The main variable of analysis of our study was based on the differential gene expression (Fold Change—FC). To achieve this, we bilaterally extracted the RTN by laser capture suction microdissection (LCM) (see workflow in Figure 3). Next, we performed mass spectrometric analysis by

Table 1. Linear model R analysis.

	F_R	$Pr(>\|t\|)$	T_V	$Pr(>\|t\|)$	M_V	$Pr(>\|t\|)$
Linear model parameters	Estimated std. error		Estimated std. error		Estimated std. error	
Intercept	103.19 ± 0.99	<0.01	8.67 ± 0.12	<0.01	913.30 ± 20.51	<0.01
Hypercapnia	46.90 ± 1.99	<0.01	3.19 ± 0.25	<0.01	873.30 ± 41.01	<0.01
Hypoxia	36.76 ± 1.99	<0.01	3.29 ± 0.25	<0.01	858.36 ± 41.01	<0.01
MCS	57.58 ± 1.99	<0.01	6.00 ± 0.25	<0.01	1463.76 ± 41.01	<0.01
PD	−19.5763 ± 1.40	<0.01	−4.63 ± 0.18	<0.01	−553.44 ± 29.00	<0.01
InteractionHypercap*PD	3.41 ± 2.81	0.229	−0.47 ± 0.36	0.196	−328.62 ± 58	<0.01
InteractionHypoxia*PD	−0.46 ± 2.81	0.870	−2.18 ± 0.36	<0.01	−600.55 ± 58	<0.01
Interaction MCS*PD	−1.71 ± 2.81	0.545	−2.68 ± 0.36	<0.01	−792.61 ± 58	<0.01
Adjusted R^2	0.9587	–	0.9580	–	0.9677	–
F-statistic	395.60	–	388.60	–	510.80	–
Residual standard error	5.46	–	0.70	–	112.3	–

Abbreviations: MCS = maximal chemorreflex stimulation (hypercapnia + hypoxia); PD = Parkinson disease group (6-OHDA); $Pr(>|t|)$ = *P*-value for that *t*-test (the proportion of the *t* distribution greater than the absolute value of *t* statistic). R Core Team (2017). R: A Language and Environment for Statistical Computing. R Foundation for Statistical Computing: Vienna, Austria. Available at: https://www.R-project.org/.

liquid chromatography-mass spectrometry (LC/MS) technique as described previously by (56). We obtained eight sections, each 12 μm in thickness, from the rostral portion of the facial nucleus, covering the entire region of the RTN. We found that the areas and tissue extracted for biomolecular analysis were similar in both groups (Figure 3A–C). Data analysis were performed using Mascot 2.6.0. Search results were compiled in Scaffold, using a 1% FDR for proteins and enabling comparison between samples. This allowed us to obtain a significant amount of protein for biomolecular analysis. We compared the levels of protein counts between the experimental and control groups and display the differential protein expression by volcano plot (Figure 3). We noted that significant skewness in the distribution of data points, with several structural proteins showing significant decrease in quantity.

The aforementioned data suggest that significant protein remodeling occurred in the RTN of PD-induced rats. To obtain insights into differential pathway activations, we performed IPA. Genes associated with cytoskeleton reorganization, protein transport, regulation of membrane traffic, regulation of Ca^{2+} homeostasis and neurotrophic factor were among the proteins showing the most dysregulation (Table 2). In Table 3, we describe the targets of each differentially expressed protein. We conclude that induction of the PD model results in both reduction of Phox2b$^+$ neurons in addition to significant biomolecular changes in the RTN region.

Pharmacological and optogenetic stimulation of remnant RTN neurons rescues PD-induced respiratory dysfunction

Having demonstrated both a reduction in Phox2b$^+$ neuron number as well as a biomolecular change in the RTN, we next tested the hypothesis that stimulation of the remnant cells could rescue the respiratory pattern of these animals. We tested the extent to which N-methyl-D-aspartate receptor (NMDAr) could activate Phox2b+ neurons by direct microinjections on RTN (Figure 4H–I). NMDA selectively binds the NMDAr, an ionotropic glutamate receptor. In nuclei associated with ventilation control, activating RTN Phox2b$^+$ glutamatergic neurons increase respiratory activity (27,70,66), whereas its blockade decreases f_R and alters breathing in adults' rats (20, 23). To verify injection site, we utilized latex microspheres to mark the injection sites. Prior to performing rescue experiments, we verified dysfunctional respiration by showing that PD mice showed a baseline reduction of f_R (81.3 ± 7.6 breaths min, vs., vehicle: 115.6 ± 12 breaths min, $P < 0.05$), V_T (3.2 ± 0.2 vs. vehicle 4.9 ± 0.7 mL/kg, $P < 0.05$) and V_E (243.9 ± 31 vs. vehicle 581.4 ± 77.6 mL/kg/min, $P < 0.05$) (Figure 4A–D). Furthermore, following the rescue experiments, we verified that SNc cells had also decreased, confirming the experimental model (368 ± 29 vs. vehicle: 1386 ± 82 neurons, $P < 0.001$).

RTN injection of NMDA in control rats increased f_R and in V_E of control animals. In the 6-OHDA group, an increase in $f_{R,}$ V_T and V_E was also observed (Figure 4A–D). The respiratory values that both groups reached during the stimulation were not different (Figure 4B–D). However, because 6-OHDA animals have resting respiratory values reduced, the delta values after the injection of NMDA in the RTN are higher in this group (f_R: 6-OHDA: Δ = +67.6 ± 25, vs. vehicle: Δ = +39.4 ± 6 breaths min, $P < 0.05$; V_T:6-OHDA: Δ = +3.7 ± 0.6, vs. vehicle: Δ = 1.3 ± 0.5 mL/kg, $P < 0.05$) (Figure 4E,F).

In order to more specifically activate Phox2b+ RTN neurons, we utilized an optegenetic approach whereby we expressed the optogenetic actuator channelrhodopsin in *Phox2b* expressing cells30. To achieve this, we utilized the PRSx8-ChR2-eYFP lentivirus, which includes a *Phox2*-binding region of the *DBH* promoter (as the RTN does not show *Phox2A* expression, *ChR2-eYFP* expression is restricted to *Phox2b*-expressing neurons). The GFP of the viral vector allowed the identification by histological analysis of the effectiveness of the infection. For photo-stimulation,

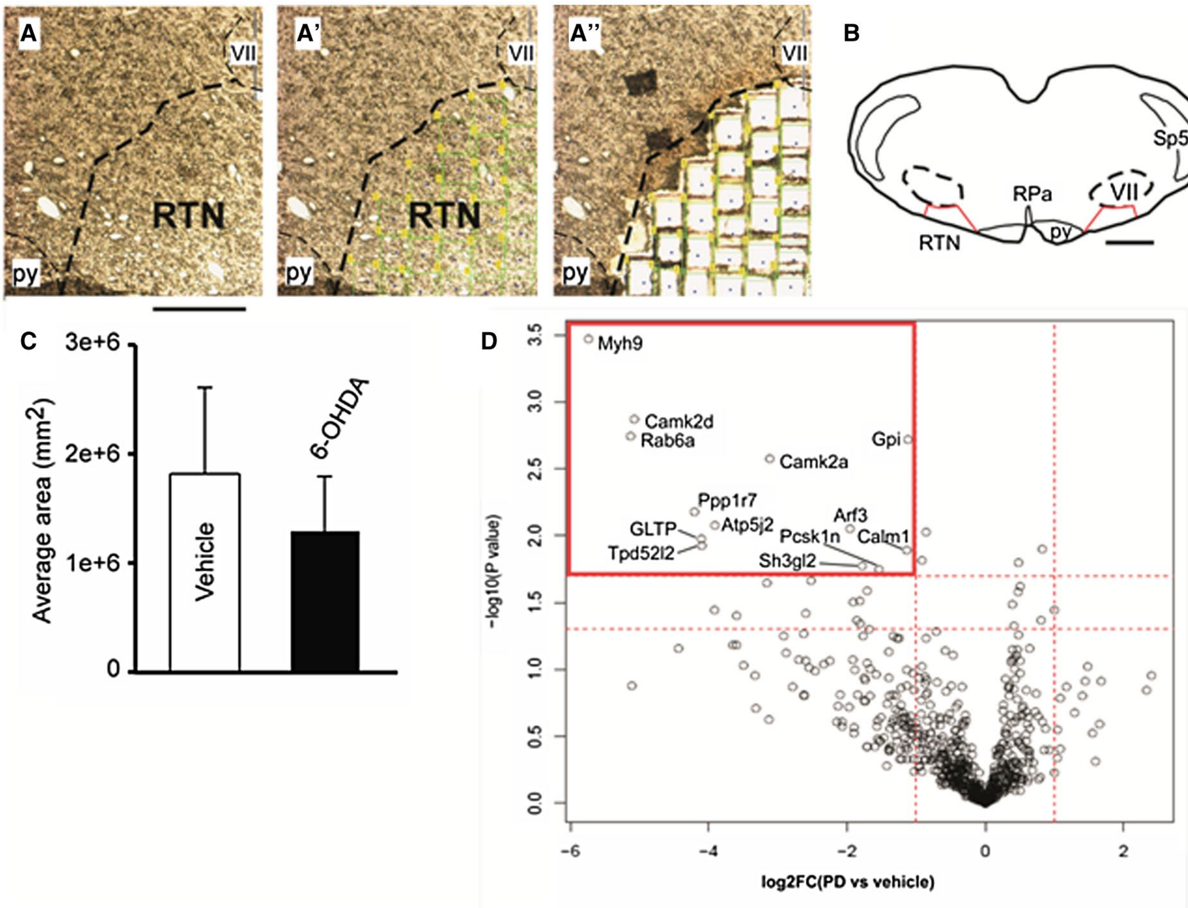

Figure 3. *Biomolecular and Volcano Plot protein analysis of RTN after induction of the experimental model of PD.* A–A″) Photomicrographs representing the area of incision of the laser (black trace, A), the slices to obtain the tissue (green squares, A′) and the biological tissue area that was capturated (A″). **B.** scheme representing the location of the microdissection area in the RTN region. **C.** Average of the areas analyzed in the RTN region 60 days after bilateral injection of vehicle or 6-OHDA (24 μg/μL). **D.** Volcano Plot showing the magnitude and significance of protein comparisons between the 6-OHDA and vehicle groups. The vertical axis indicates the log10 (*P* value) and the horizontal axis indicates log2 (fold change- FC). The red square indicates the points that display changes (FC) of great magnitude (*x* axis), as well as high statistical significance (−log10 of the *P* value, *y* axis). The points located in the dashed red line have $P = 0.05$, the points located above have $P < 0.05$ and the points located below have $P > 0.05$). One-way analysis of variance (ANOVA) ($P = 0.06$) (average area) and two-way analysis (Volcano Plot). Data displayed as mean ± SD. Abbreviations: py = pyramid; RPa = raphe pallidus area; RTN = retrotrapezoid nucleus; Sp5 = trigeminal spinal tract; VII = motor nucleus of the facial nerve. Scale in A = 300 μm (applies to A′–A″) and B = 1.0 mm.

we used the same animals in two conditions: non-anesthetized and anesthetized. In non-anesthetized animals, we accessed the RTN region from guide cannulas implanted in the dorsal region of the skull, allowing the animals to move freely in the plethysmography chamber (22,63) and in anesthetized animals the access was performed with a stereotaxic frame coupled cannula, targeting the RTN ventrally. In the non-anesthetized animals, the photo-stimulation of the RTN increased V_T (ON: 5.4 ± 1.7, vs. OFF: 3.6 ± 1.1 ml/kg, $P < 0.05$), and V_E (ON: 477 ± 166, vs. OFF: 294 ± 11 mL/kg/min, $P < 0.05$), without changing the f_R in vehicle animals (Figure 5A–D). In the 6-OHDA animals, the same selective stimulation increased f_R (ON: 111 ± 22, vs. OFF: 88 ± 12 breaths min, $P < 0.05$) and V_E (ON: 494 ± 92, vs. OFF: 371 ± 85 mL/kg/min, $P < 0.05$) (Figure 5A–D). We also plotted the effect of stimulation by the percentage of RTN lesion and *Phox2b* expressing neurons infected (Figure 5F,G). It is important to note that the higher response was observed in the animal that presented lesions below 40% of the Phox2b neurons in the RTN (Figure 5E) and there is a higher response in the V_E associated with higher percentages of infected neurons in 6-OHDA animals (Figure 5F).

We also performed the photo-stimulation of anesthetized animals. Under anesthetic conditions, the 6-OHDA animals also present a reduction of basal f_R (30.3 ± 2 vs. vehicle: 36.8 ± 5 breaths min, $P < 0.05$, Figure 6A,B) and both groups did not show abdominal muscular activation while

Table 2. Top list of differentiated proteomes: predicted upstream regulators and downstream effectors. Proteins are sorted by their gene name.

Gene symbol	Summarized functions	Location	Differential gene expression	Fold change (V × PD)	*P*-value
Myh9	Cellular myosin that appears to play a role in cytokinesis, cell shape, and specialized functions such as secretion and capping. During cell spreading, plays an important role in cytoskeleton reorganization	Cytoskeleton	Down-regulation	5.74	0.00034
Rab6A	Protein transport. Regulator of membrane traffic from the Golgi apparatus towards the endoplasmic reticulum (ER). Involved in COPI-independent retrograde transport from the Golgi to the ER	Golgi apparatus	Down-regulation	5.08	0.00135
Camk2D	Calcium/calmodulin-dependent protein kinase involved in the regulation of Ca^{2+}homeostatis and excitation-contraction coupling (ECC) in heart by targeting ion channels, transporters and accessory proteins involved in Ca^{2+} influx into the myocyte, Ca^{2+} release from the sarcoplasmic reticulum (SR), SR Ca^{2+} uptake and Na^+ and K^+ channel transport	Plasma membrane and nucleus	Down-regulation	5.13	0.00179
Gpi	Besides it's role as a glycolytic enzyme, mammalian Gpi can function as a tumor-secreted cytokine and an angiogenic factor (AMF) that stimulates endothelial cell motility. Gpi is also a neurotrophic factor (Neuroleukin) for spinal and sensory neurons	Extracellular region or secreted and cytoplasm	Up-regulation	1.12	0.00191
Camk2A	CaM-kinase II (CAMK2) is a prominent kinase in the central nervous system that may function in long-term potentiation and neurotransmitter release. Member of the NMDAR signaling complex in excitatory synapses it may regulate NMDAR-dependent potentiation of the AMPAR and synaptic plasticity. Phosphorylates transcription factor FOXO3 on "Ser-298". Activates FOXO3 transcriptional activity	Plasma membrane, presynaptic cell membrane	Up-regulation	3.12	0.00268
Ppp1r7	Regulatory subunit of protein phosphatase 1	Nucleus	Down-regulation	4.21	0.00665
Atp5j2	Mitochondrial membrane ATP synthase (F1F0 ATP synthase or Complex V) produces ATP from ADP in the presence of a proton gradient across the membrane which is generated by electron transport complexes of the respiratory chain	Mitochondrion	Down-regulation	3.91	0.00831
Arf3	GTP-binding protein that functions as an allosteric activator of the cholera toxin catalytic subunit, an ADP-ribosyltransferase. Involved in protein trafficking	Golgi apparatus	Up-regulation	1.96	0.00888
Calm1	Calmodulin mediates the control of a large number of enzymes, ion channels, aquaporins and other proteins through calcium-binding. Together with CCP110 and centrin, is involved in a genetic pathway that regulates the centrosome cycle and progression through cytokinesis. Mediates calcium-dependent inactivation of CACNA1C. Positively regulates calcium-activated potassium channel activity of KCNN2	Cytoskeleton	Up-regulation	0.86	0.00947

(Continues)

Table 2. (Continued)

Gene symbol	Summarized functions	Location	Differential gene expression	Fold change (V × PD)	*P*-value
GLTP	Accelerates the intermembrane transfer of various glycolipids. Catalyzes the transfer of various glycosphingolipids between membranes but does not catalyze the transfer of phospholipids. May be involved in the intracellular translocation of glucosylceramides	Cytoplasm	Down-regulation	4.11	0.01054
Tpd52l2	Known to be associated with tumor growth. Currently classified as *Protein existence* (indicates the type of evidence that supports the existence of the protein)	Cytoplasm	Down-regulation	4.1	0.01187
Pcsk1n	May function in the control of the neuroendocrine secretory pathway. Proposed be a specific endogenous inhibitor of Pcsk1. May control the intracellular timing of Pcsk1 rather than its total level of activity	Golgi apparatus	Up-regulation	0.82	0.01254
Sh3gl2	Catalytic function. Phosphatase that acts on various phosphoinositides, including phosphatidylinositol 4-phosphate, phosphatidylinositol (4,5)-bisphosphate and phosphatidylinositol (3,4,5)-trisphosphate (By similarity). Has a role in clathrin-mediated endocytosis	Cytosol and plasma membrane	Up-regulation	1.14	0.01291

the laser was in OFF condition (Figure 6A). In the control animals, photo-stimulation produced no changes in inspiratory parameters but was able to generate active expiration (Figure 6A–G). In 6-OHDA group, photo-stimulation promoted an increase in frequency (ON: 42.5 ± 4 vs. OFF: 30.5 ± 2 breaths min, $P < 0.05$) and amplitude (ON: 0.22 ± 0.04, vs. OFF: 0.17 ± 0.04 mV, $P < 0.05$) of the diaphragm muscle and increased electrical activity of the abdominal muscles, demonstrating that light pulses were also able to generate active expiration (Figure 6A–G). In this group of animals, the best responses in f_R occurred in animals with less than 60% lesion in the RTN (Figure 6H) and the higher percentage of transfected neurons was associated with higher f_R responses during photo-stimulation, especially in animals submitted to the experimental model for PD (Figure 6I). We monitored the blood pressure (BP) of the animals throughout the experiments under anesthesia and the photo-stimulation did not produce changes in resting BP in both groups of animals (data not shown).

We verified RTN pathology following these experiments by immunohistochemical labeling for Phox2b. We confirmed, in the range between 11.36 and 11.6 mm caudal to bregma, a reduction of the neurons of the RTN region in the animals submitted to the 6-OHDA experimental model (27 ± 2, vs. vehicle 54 ± 10 neurons, $P < 0.01$) and an equivalent proportion of transfected neurons between the groups (data not shown). We conclude that despite the presence of significant neurodegenerative changes that reduce RTN number, that the remaining *Phox2b*-expressing RTN neurons, if activated exogenously, could restore respiratory physiology.

DISCUSSION

In the present study, we set out to evaluate the extent to which SNc degeneration induced biomolecular changes in the RTN and to identify the extent to which RTN pharmacological or optogenetic stimulations could rescue respiratory function. We demonstrate that in addition RTN Phox2b-expressing neuron reduction, that the RTN region shows significant biomolecular changes. Furthermore, we note that exogenous stimulation of the RTN, either by local NMDA treatment or optogenetic stimulation of Phox2b-expressing neurons, rescued respiratory dysfunction.

Respiratory changes in an experimental PD model

SNc dopaminergic neuron degeneration suppresses eupneic breathing in adult rats. It has been shown in the literature that the onset of neurodegeneration in PD patients can be observed in medullary regions, such as the locus coeruleus, dorsal motor nucleus of the vagus and regions associated with respiratory control (13). Hypoxia ventilatory response (HVR) is a complex interaction between several distinct mechanisms whose variations depend on

Table 3. Predicted state of molecules (up-stream analysis) of the experimental (PD) in relation to the control group (vehicle).

Gene symbol	Type (s)	Predicted state	Activation *z*-score	*P*-value of overlap	Target molecules
ADORA2A	G-protein receptor	Inhibited	−3.317	0.000000211	Arf3, Gpi, Rab6A
INSR	kinase	Inhibited	−2.804	0.000000389	Calm1, Atp5j2
SRF	Transcription regulator	Inhibited	−2.232	0.00126	Myh9, RNH1, Tpm1, Tpm2
PPARGC1A	Transcription regulator	Inhibited	−2.025	0.00147	Atp5j2, AK1
ESR1	Ligand-dependent nuclear receptor	Inhibited	−2.132	0.0021	Rab6A, MAPK1, AK1
IGF1	Growth factor	Inhibited	−2.847	0.00596	GPD1, MAPK1, Myh9, Myh11
AGT	Growth factor	Inhibited	−2.172	0.0104	ANXA3, Calm1, Myh10
NFE2L2	Transcription regulator	Inhibited	−3.913	0.000000211	Calm1, Tpm1
RICTOR	Kinases mediate responses to stresses	Activated	3.79	1.31e−19	Atp5j2
CD 437	Chemical drug	Activated	2.828	1.25e−11	Atp5j2, EEF2
ST1926	Chemical drug	Activated	2.138	3.1e−09	Atp5j2, EEF2
MAP4K4	Kinase	Activated	2.813	0.000047	ACAA2, Calm1, FASN
mir-1	Microrna	Activated	2.433	0.000197	
DNMT3B	Enzyme	Activated	2	0.00299	ATP2A2, CAMK2A, EPDR1, MYL6
PD98059	Kinase inhibitor	Activated	2.074	0.003	ACAT2,ALDOA,AP2B1, Gpi, MAPK1, MYH11
DNMT3A	Enzyme	Activated	2	0.0114	ATP2B4, CAMK2A, CKM, ENPP6, KCNA1
mir-122	Microrna	Activated	2	0.0159	ALDOA, TPD52L2

the stimulus pattern, duration and intensity of hypoxia exposure. In longer episodes, ventilation has a biphasic pattern (11). In our experiments, in the first minutes (1–2 minutes) after O_2 reduction, the animals presented a considerable increase in ventilation, presumably by a reflex response to the activation of peripheral receptors located in the carotid body. This response was reduced in the animals submitted to the experimental model of PD. We also decided to perform the MCS and it was possible to observe that even in these extreme conditions, the animals submitted to the PD model presented ventilatory deficit when compared to the control animals.

Neuroanatomical and biomolecular changes in an experimental PD model

In most PD patients, several debilitating symptoms occur before, simultaneously or after the onset of classic motor symptoms, such as sleep pathologies, cognitive and psychiatric deficits, and respiratory, sensorial and autonomic dysfunctions (9, 19, 21). These symptoms may have an even greater negative impact on quality of life when compared to the classic aspects of PD (43). As stated, patients with PD may present respiratory impairment; however, data that link respiratory control to these changes are still scarce. A study conducted by Budzinska and Andrzejewski also reported respiratory deficits in a PD model with unilateral administration of 6-OHDA in rats anesthetized and artificially ventilated (16). Seccombe *et al* (2011) suggest that respiratory changes may be associated with a dysfunction of respiratory neurons. Although these authors observed in PD patients respiratory muscle weakness, the changes were insufficient to cause any significant impairment in ventilation (58). Previous studies have also identified that in rat PD models, there is a reduction in breathing with corresponding pathologies in respiratory control centers including RTN, preBötzinger Complex (preBötC), NTS and rostral ventral respiratory group (rVRG) (24-26,47,67).

The changes observed in the proteomic analyses, as well as the estimated effect according to the degree of statistical confidence, enabled us to list 13 main altered proteins in PD-induced rat RTN. We found increased RNH1 levels, a protein known to negatively regulate signaling cascades that mediate the activation of MAP kinases and TPP2 (73). Deregulation of these enzymes is associated with changes in cell proliferation, glycogen metabolism and neurotransmission in the CNS (14). We also observed that CAMK2a kinase, prominent in the CNS acting on long-term potentiation and neurotransmitter release, showed increased levels in PD-induced rats. This enzyme belongs to the receptor signaling complex for NMDAr (NMDAr) in excitatory synapses and can regulate the potentiation of NMDAr-dependent glutamatergic receptor-AMPA (AMPAr) and synaptic plasticity (5, 36). MYH9 and CAMK2d showed decreased levels. MYH9 is a cellular myosin with role in cytokinesis and cell shape. During cell proliferation, it plays an important role in the reorganization of the cytoskeleton (72). In contrast, the CAMK2a protein is involved in the regulation of Ca^{2+} homeostasis (36). In sum, the results obtained by mass spectrometry and proteomics demonstrated a protein remodeling in the RTN region after bilateral injections of 6-OHDA in CPu, suggesting that the experimental model of PD

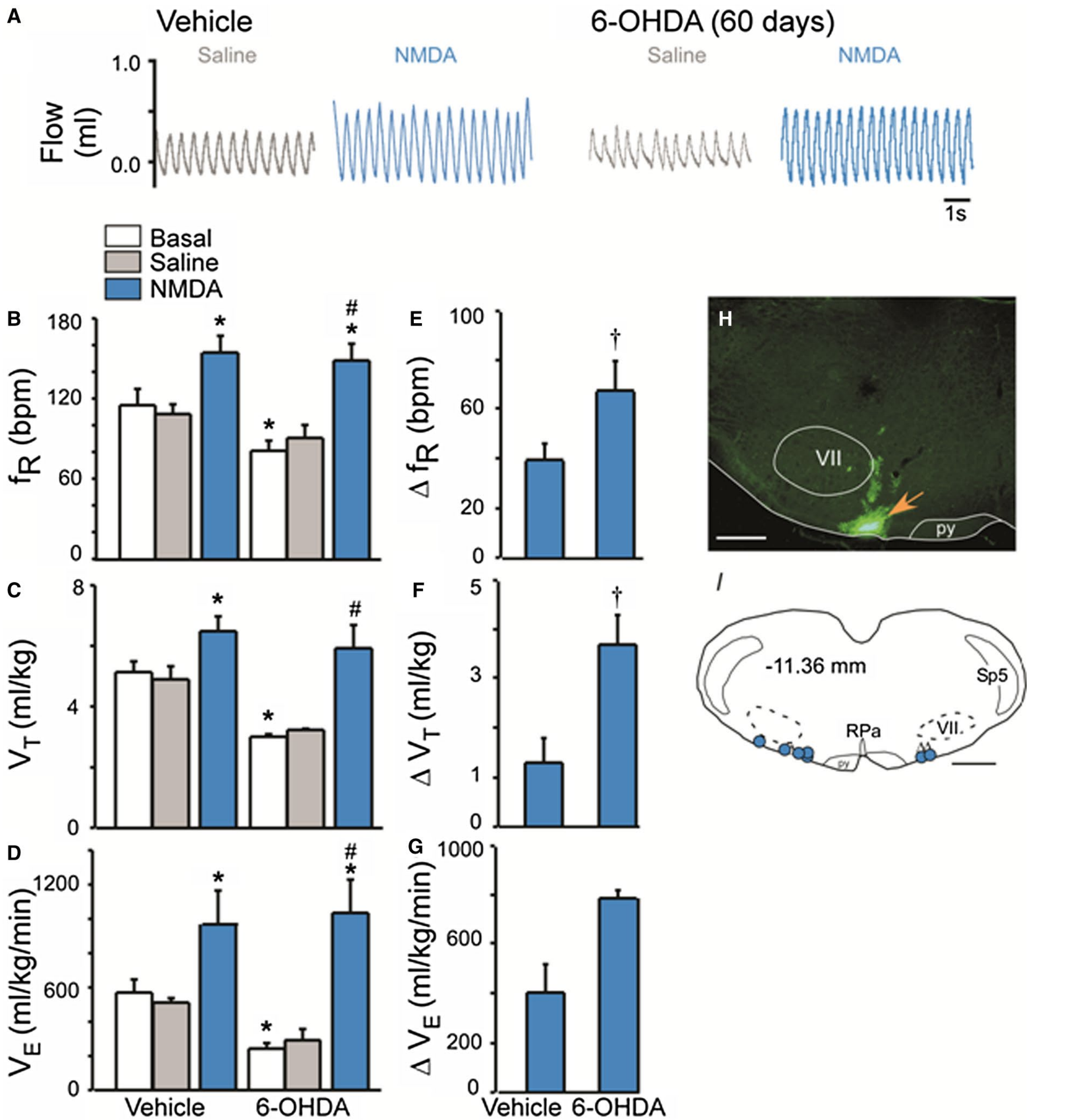

Figure 4. *Pharmacological stimulation of RTN neurons after induction of the experimental model of PD.* (**A**) Typical recordings showing increased respiratory flow after injection of NMDA (5 pmol/50 nL) in RTN 60 days after bilateral injection of vehicle or 6-OHDA (24 µg/µL) in CPu. Changes in (**B** and **E**) f_R, (**C** and **F**) V_T and (**D** and **G**) V_E produced by injection of NMDA in RTN 60 days after bilateral injection of vehicle or 6-OHDA (24 µg/µL) in CPu. (**H**) Photomicrograph showing the location of NMDA injection in the RTN region of an animal of the 6-OHDA group, (**I**) schematic representation of the location of the injections in the vehicle and 6-OHDA animals (Bregma = −11.36 mm). One-way ANOVA followed by Tukey's post hoc test was used. $^{*}P < 0.05$ in relation to the baseline moment of the vehicle group; $^{\#}P < 0.05$ in relation to the baseline time of the 6-OHDA group; $^{\dagger}P < 0.05$ in relation to the NMDA moment of the vehicle group. Abbreviations: py = piramidal tract; RPa = raphe pallidus area; Sp5 = trigeminal spinal tract; VII = motor nucleus of the facial nerve. Scales in H = 0.5 mm and I = 1.0 mm.

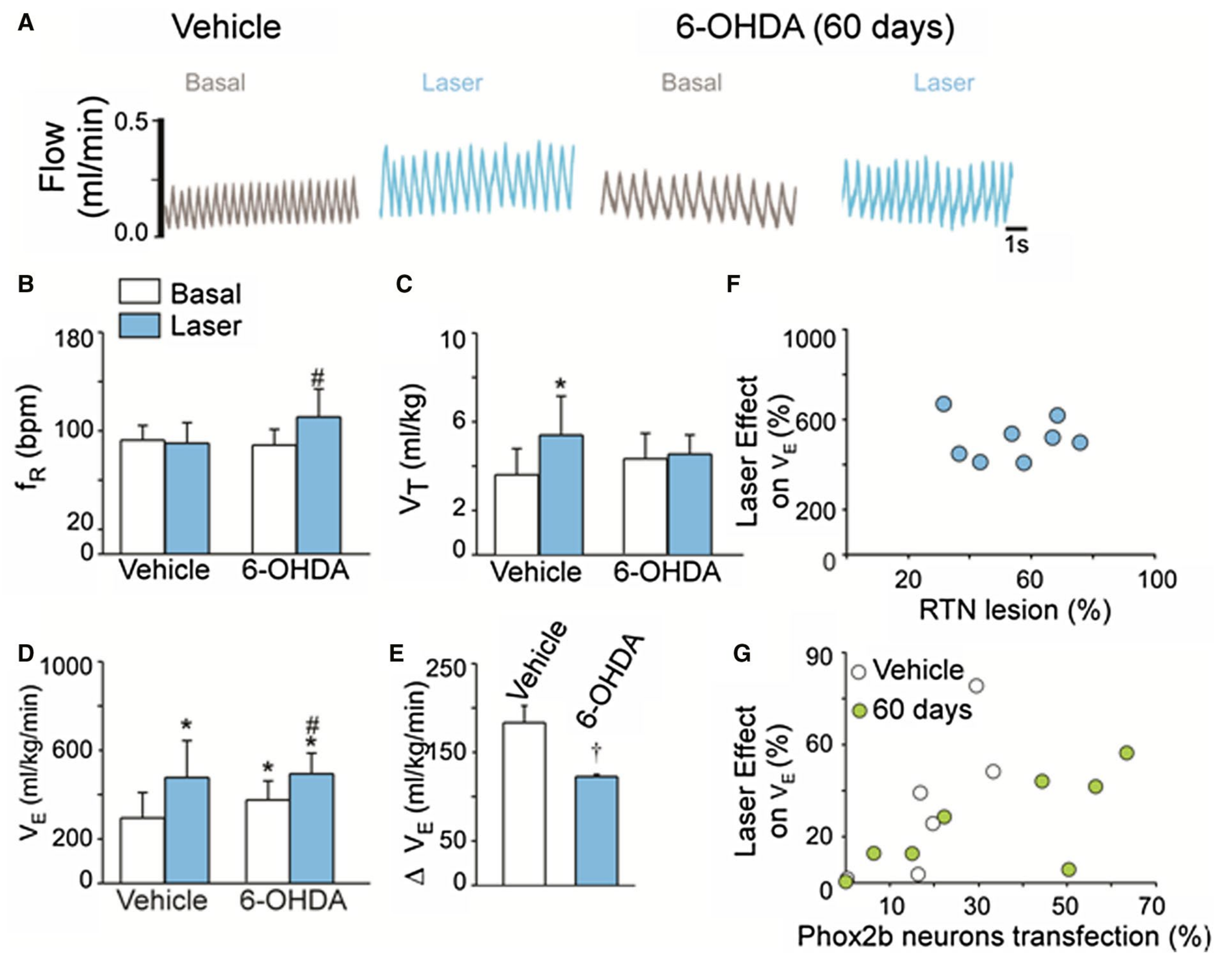

Figure 5. *Optogenetic stimulation of Phox2b neurons in non-anesthetized animalsafter induction of the experimental model of PD.* **A.** Typical recordings showing increased respiratory flow after photo-stimulation of Phox2b neurons in RTN 60 days after bilateral injection of vehicle or 6-OHDA (24 µg/µL) in CPu. Changes in (**B**) f_R, (**C**) V_T and (**D**) and (**E**) V_E produced by photo-stimulation of Phox2b neurons in RTN 60 days after bilateral injection of vehicle or 6-OHDA (24 µg/µL) in CPu. Relation between the percentage of lesion (**F**) and transfected neurons in the RTN (G) with the effect of photo-stimulation on the V_E (Vehicle: white circle,6-OHDA: green circle). One-way ANOVA followed by Tukey's post hoc test was used. $^*P < 0.05$ in relation to the vehicle group at baseline. $^{\#}P < 0.05$ in relation to the 6-OHDA group at baseline.

can alter the biomolecular pattern in areas critical for respiratory neural control.

Pharmacological and optogenetic stimulation of the RTN region in a PD model

The neuromodulation of deep brain structures (deep brain stimulation) represents an effective therapeutic intervention for PD patients with movement disorders (41). As a proof of principal, we utilized optogenetic stimulation to test if exogenous administration of remaining RTN neurons could rescue respiratory dysfunction. A recent study demonstrated that optogenetic activation of the secondary motor cortex (M2) reversed motor disorders in male mice with dopamine depletion (41). In our study, by injecting unilaterally the viral vector in the RTN in PD model, we were able to selectively stimulate this region in anesthetized animals, as well as in physiological conditions free of anesthesia. The data obtained in this study provided the first evidence that even with a reduction in the number of Phox2b neurons in the RTN and with a biomolecular signature demonstrating a process of protein remodeling, the pharmacological and optogenetic stimulation of this region were able to potentiate the baseline ventilatory response. These data show proof of concept that neuromodulation may improve the non-movement disorders in PD.

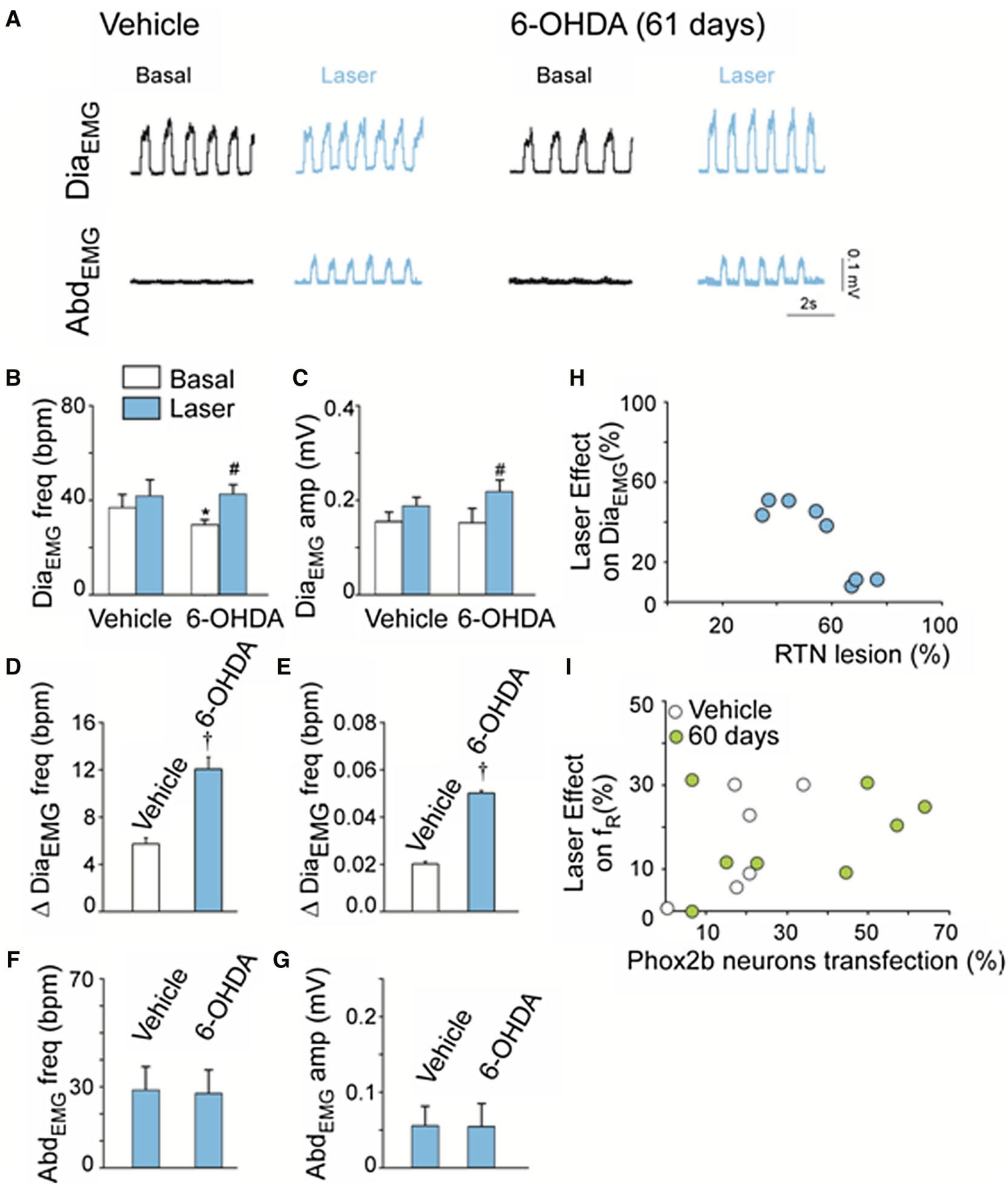

Figure 6. *Optogenetic stimulation of Phox2b neurons in anesthetized animals after induction of the experimental model of PD.* **A.** Typical recording showing increased diaphragm and abdominal muscle activities during the photo-stimulation (30 mW) of Phox2b neurons in RTN 60 days after bilateral injection of vehicle or 6-OHDA (24 μg/μL) in CPu. Changes in diaphragm muscle (**B** and **D**) frequency and (**C** and **E**) amplitude and abdominal muscle (**F**) frequency and (**G**) amplitude. Relation between the percentage of lesion (**H**) and transfected neurons (**I**) in the RTN and the effect of the photo-stimulation in the frequency. One-way ANOVA followed by Tukey's post hoc test was used. $^*P < 0.05$ in relation to the vehicle group at baseline. $^\#P < 0.05$ in relation to the 6-OHDA group at baseline. Data displayed as mean ± SD.

ACKNOWLEDGMENTS

This research was supported by Serrapilheira Institute (Grant: Serra-1812-26431), public funding from São Paulo Research Foundation (FAPESP) (Grants: 2016/23281-3 to ACT; 2015/23376-1 to TSM), Conselho Nacional de Desenvolvimento Científico e Tecnológico (CNPq) (grants: 408647/2018-3 to ACT) and by funds from FAPESP fellowship (2014/20695-6 and 2017/11165-1 to SAFJ), CNPq fellowship to SAFJ, TSM (301904/2015-4) and ACT (301219/2016-8), National Institutes of Health NIH/NHLBI to CMC and JJO (R01HL132355), NIH/NINDS (P30 NS045758, RN). The project described was supported by Award Number UL1TR001070 from the National Center for Advancing Translational Sciences. The content is solely the responsibility of the authors and does not necessarily represent the official views of the National Center for Advancing Translational Sciences or the National Institutes of Health. This study was financed in part by the Coordenação de Aperfeiçoamento de Pessoal de Nível Superior—Brazil (CAPES)—Finance Code 001.

AUTHOR CONTRIBUTIONS

TSM, JJO, SAFJ, CC, SR, SA and ACT designed and interpreted the experiments; SAFJ, LMO, CC, LMO, MX, ZL and ACT collected and analyzed data; SAFJ, TSM, CC, JJO and ACT wrote the paper. All authors have read and approved the final version of the manuscript and agree to be accountable for all aspects of the work in ensuring that questions related to the accuracy or integrity of any part of the work are appropriately investigated and resolved. All persons designated as authors qualify for authorship, and all those who qualify for authorship are listed.

COMPETING INTERESTS

The authors have no conflicts of interest to disclose.

DATA AVAILABILITY STATEMENT

Data available on request from the authors. The data that support the findings of this study are available from the corresponding author, [ACT], upon reasonable request.

REFERENCES

1. Abbott SB, Stornetta RL, Socolovsky CS, West GH, Guyenet PG (2009) Photostimulation of channelrhodopsin-2 expressing ventrolateral medullary neurons increases sympathetic nerve activity and blood pressure in rats. *J Physiol* **587**(Pt 23):5613–5631.
2. Abbott SB, Stornetta RL, Fortuna MG, Depuy SD, West GH, Harris TE, Guyenet PG (2009) Photostimulation of retrotrapezoid nucleus phox2b-expressing neurons in vivo produces long-lasting activation of breathing in rats. *J Neurosci* **29**:5806–5819.
3. Abbott SB, Kanbar R, Bochorishvili G, Coates MB, Stornetta RL, Guyenet PG (2012) C1 neurons excite locus coeruleus and A5 noradrenergic neurons along with sympathetic outflow in rats. *J Physiol* **590**:2897–2915.
4. Abbott SB, Coates MB, Stornetta RL, Guyenet PG (2013) Optogenetic stimulation of C1 and retrotrapezoid nucleus neurons causes sleep state dependent cardiorespiratory stimulation and arousal in rats. *Hypertension* **61**, 835–841.
5. Akita T, Aoto K, Kato M, Shiina M, Mutoh H, Nakashima M *et al* (2018) De novo variants in CAMK2A and CAMK2B causes neurodevelopmental disorders. *Ann ClinTransl Neurol* **5**:280–296.
6. Anderson TM, Garcia AJ, Baertsch NA, Pollak J, Bloom JC, Wei AD *et al* (2016) A novel excitatory network for the control of breathing. *Nature* **536**:76–80.
7. Aravanis AM, Wang LP, Zhang F, Meltzer LA, Mogri MZ, Schneider MB, Deisseroth C (2007) An optical neural interface: in vivo control of rodent motor cortex with integrated fiberoptic and optogenetic technology. *J Neural Eng* **4**:S143–S156.
8. Baertsch NA, Baertsch HC, Ramirez JM (2018) The interdependence of excitation and inhibition for the control of dynamic breathing rhythms. *Nat Commun* **9**:843.
9. Bassetti CL (2011) Nonmotor disturbances in Parkinson's disease. *Neurodegener Dis* **8**:95–108.
10. Benjamini Y, Hochberg Y (1995) Controlling the false discovery rate: a practical and powerful approach to multiple testing. *J R Stat Soc Ser B Stat Methodol* **57**:289–300.
11. Blain GM, Smith CA, Henderson KS, Dempsey JA (2010) Peripheral chemoreceptors determine the respiratory sensitivity of central chemoreceptors to CO2. *J Physiol* **588**(Pt 13):2455–2471.
12. Blum D, Torch S, Lambeng N, Nissou M, Benabid AL, Sadoul R, Verna JM (2001) Molecular pathways involved in the neurotoxicity of 6-OHDA, dopamine and MPTP: contribution to the apoptotic theory in Parkinson's disease. *Prog Neurobiol* **65**:135–172.
13. Braak H, Del Tredici K, Rüb U, de Vos RAI, Jansen Steur ENH, Braak E (2003) Staging of brain pathology related to sporadic Parkinson's disease. *Neurobiol Aging* **24**:197–211.
14. Bright R, Mochly-Rosen D (2005) The role of protein kinase C cerebral ischemic and reperfusion injury. *Stroke* **36**:2781–2790.
15. Bruinstroop E, Cano G, Vanderhorst VG, Cavalcante JC, Wirth J, Sena-Esteves M, Saper CB (2012) Spinal projections of the A5, A6 (locus coeruleus), and A7 noradrenergic cell groups in rats. *J Comp Neurol* **520**:1985–2001.
16. Budzinska K, Andrzejewski K (2014) Respiratory activity in the 6-OHDA hydroxydopamine model of Parkinson's disease in the rat. *Acta Neurobiol Exp (Wars)* **74**:67–81.
17. Card JP, Sved JC, Craig B, Raizada M, Vazquez J, Sved AF (2006) Efferent projections of rat rostroventrolateral medulla C1 catecholamine neurons: implications for the central control of cardiovascular regulation. *J Comp Neurol* **499**:840–859.
18. Colinge J, Chiappe D, Lagache S, Moniatte M, Bougueleret L (2005) Differential proteomics via probabilistic peptide identification scores. *Anal Chem* **77**:596–606.
19. Chaudhuri KR, Odin P, Antonini A, Martinez-Martin P (2011) Parkinson's disease: the non-motor issues. *Parkinsonism Relat Disord* **17**:717–723.
20. Connelly CA, Otto-Smith MR, Feldman JL (1992) Blockade of NMDA receptor-channels by MK-801 alters breathing in adult rats. *Brain Res* **596**:99–110.
21. Cummings JL (1992) Depression and Parkinson's disease: a review. *Am J Psychiatry* **149**:443–454.
22. Deisseroth K, Feng G, Majewska AK, Miesenböck G, Ting A, Schnitzer MJ (2006) Next-generation optical technologies for illuminating genetically targeted brain circuits. *J Neurosci* **26**:10380–10386.
23. Dzal YA, Seow A, Borecky LG, Chung D, Gill SKG, Milsom WK, Pamenter ME (2019) Glutamatergic receptors modulatenormoxic but not hypoxic ventilationand metabolism in naked mole rats. *Front Physiol* **10**:106.

24. Falquetto B, Tuppy M, Potje RS, Moreira TS, Antoniali C, Takakura AC (2017) Cardiovascular dysfunction associated with neurodegeneration in an experimental model of Parkinson's disease. *Brain Res* **1657**:156–166.
25. Favero MT, Takakura AC, de Paula PM, Colombari E, Menani JV, Moreira TS (2011) Chemosensory control by commissural nucleus of the solitary tract in rats. *Respir Physiol Neurobiol* **179**:227–234.
26. Fernandes-Junior SA, Carvalho KS, Moreira TS, Takakura AC (2018) Correlation between neuroanatomical and functional respiratory changes observed in an experimental model of Parkinson's disease. *Exp Physiol* **103**:1377–1389.
27. Gonda X (2012) Basic pharmacology of NMDA receptors. *Curr Pharm Des* **18**:1558–1567.
28. Haralick RM, Shanmugam K, Dinstein I (1973) Textural features for image classification. *IEEE T Syst Man Cyb Smc* **3**:610–621.
29. Howard CV, Reed MG (1998) Three-Dimensional Measurement in Microscopy. Unbiased Stereology. Springer: New York.
30. Josselyn SA (2018) The past, present and future of light-gated ion channels and optogenetics. *eLife* **7**:e42367.
31. Kanbar R, Stornetta RL, Cash DR, Lewis SJ, Guyenet PG (2010) Photostimulation of Phox2b medullary neurons activates cardiorespiratory function in conscious rats. *Am J Respir Crit Care Med* **182**:1184–1194.
32. Katagiri T, Hatano N, Aihara M, Kawano H, Okamoto M, Liu Y *et al* (2010) Proteomic analysis of proteins expressing in regions of rat brain by a combination of SDS-PAGE with nano-liquid chromatography quadrupole-time of flight tandem mass spectrometry. *Proteome Sci* **8**:41.
33. Tieu K (2011) A guide to neurotoxic animal models of Parkinson's disease. *Cold Spring Harb Perspect Med* **1**:a009316.
34. Kuhn M (2019) caret: Classification and Regression Training, pp. record ascl:1505.003. Astrophysics Source Code Library: The SAO/NASA Astrophysics Data System: Cambridge, MA.
35. Kursa MB, Rudnicki WR (2010) Feature selection with the Boruta package. *J Stat Softw* **36**:1–13.
36. Kury S, van Woerden GM, Besnard T, Onori MP, Latypova X, Towne MC *et al* (2017) De novo mutations in protein kinase genes CAMK2A and CAMK2B cause intellectual disability. *Am J Human Genet* **101**:768–788.
37. Liaw A, Wiener M (2002) Classification and regression by randomForest. *R News* **2002**:18–22.
38. Lima JC, Oliveira LM, Botelho MT, Moreira TS, Takakura AC (2018) The involvement of the pathway connecting the substantia nigra, the periaqueductal gray matter and the retrotrapezoid nucleus in breathing control in a rat model of Parkinson's disease. *Exp Neurol* **302**:46–56.
39. Liu H, Sadygov RG, Yates JR III (2004) A model for random sampling and estimation of relative protein abundance in shotgun proteomics. *Anal Chem* **76**:4193–4201.
40. Lyck L, Santamaria ID, Pakkenberg B, Chemnitz J, Schroder HD, Finsen B, Gundersen HJ (2009) An empirical analysis of the precision of estimating the numbers of neurons and glia in human neocortex using a fractionator-design with sub-sampling. *J Neurosci Methods* **182**:143–156.
41. Magno LAV, Tenza-Ferrer H, Collodetti M, Aguiar MFG, Rodrigues APC, da Silva RS *et al* (2019) Optogenetic stimulation of the M2 cortex reverts motor dysfunction in a mouse model of Parkinson's disease. *J Neurosci* **39**:3234–3248.
42. Malheiros-Lima MR, Totola LT, Lana MVG, Strauss BE, Takakura AC, Moreira TS (2018) Breathing responses produced by optogenetic stimulation of adrenergic C1 neurons are dependent on the connection with preBötzinger complex in rats. *Pflugers Arch* **470**:1659–1672.
43. Martinez-Martin P (2011) The importance of non-motor disturbances to quality of life in Parkinson's disease. *J Neurol Sci* **310**:12–16.
44. Menuet C, Sevigny CP, Connelly AA, Bassi JK, Jancovski N, Williams DA *et al* (2014) Catecholaminergic C3 neurons are sympathoexcitatory and involved in glucose homeostasis. *J Neurosci* **34**:15110–15122.
45. Mulkey DK, Stornetta RL, Weston MC, Simmons JR, Parker A, Bayliss DA, Guyenet PG (2004) Respiratory control by ventral surface chemoreceptor neurons in rats. *Nat Neurosci* **7**:1360–1369.
46. Nair-Roberts RG, Chatelain-Badie D, Benson E, White-Cooper H, Bolam JP, Ungless MA (2008) Stereological estimates of dopaminergic, gabaergic and glutamatergic neurons in the ventral tegmental area, substantianigra and retrorubral field in the rat. *Neuroscience* **152**:1024–1031.
47. Nattie EE, Li A (2008) Muscimol dialysis into the caudal aspect of the nucleus tractus solitarii of conscious rats inhibits chemoreception. *Respir Physiol Neurobiol* **164**:394–400.
48. Oliveira LM, Moreira TS, Kuo FS, Mulkey DK, Takakura AC (2016) α1- and α2- adrenergic receptors in the retrotrapezoid nucleus differentially regulate breathing in anesthetized adult rats. *J Neurophysiol* **116**:1036–1048.
49. Oliveira LM, Tuppy M, Moreira TS, Takakura AC (2017) Role of the locus coeruleus catecholaminergic neurons in the chemosensory control of breathing in a Parkinson's disease model. *Exp Neurol* **293**:172–180.
50. Parkinson J (2002) An essay on the shaking palsy. 1817. *J Neuropsychiatry Clin Neurosci* **14**:223–236; discussion 222.
51. Pau G, Fuchs F, Sklyar O, Boutros M, Huber W (2010) EBImage–an R package for image processing with applications to cellular phenotypes. *Bioinformatics* **26**:979–981.
52. Paxinos G, Watson C (1998) The Rat Brain in Stereotaxic Coordinates. Academic Press: New York.
53. R Core Team (2017) R: A language and environment for statistical computing. R Foundation for Statistical Computing: Vienna, Austria. Available at: https://www.R-project.org/. Accessed February 09, 2020.
54. Robinson MD, McCarthy DJ, Smyth GK (2010) edgeR: a bioconductor package for differential expression analysis of digital gene expression data. *Gene Expr* **26**:139–140.
55. Ross-Macdonald P, Coelho PS, Roemer T, Agarwal S, Kumar A, Jansen R *et al* (1999) Large-scale analysis of the yeast genome by transposon tagging and gene disruption. *Nature* **402**:413–418.
56. Roy S, Sen CK (2013) Study of the human chronic wound tissue: addressing logistic barriers and productive use of laser capture microdissection. *Methods Mol Biol* **1037**:233–243.
57. Schreihofer AM, Guyenet PG (1997) Identification of C1 presympathetic neurons in rat rostral ventrolateral medulla by juxtacellular labeling in vivo. *J Comp Neurol* **387**:524–536.
58. Seccombe LM, Giddings HL, Rogers PG, Corbett AJ, Hayes MW, Peters MJ, Veitch EM (2011) Abnormal ventilatory control in Parkinson's disease–further evidence for non-motor dysfunction. *Respir Physiol Neurobiol* **179**:300–304.

59. Shapiro JP, Biswas S, Merchant AS, Satoskar A, Taslim C, Lin S *et al* (2012) A quantitative proteomic workflow for characterization of frozen clinical biopsies: laser capture microdissection coupled with label-free mass spectrometry. *J Proteomics* **77**:433–440.
60. Silva JN, Tanabe FM, Moreira TS, Takakura AC (2016) Neuroanatomical and physiological evidence that the retrotrapezoid nucleus/parafacial region regulates expiration in adult rats. *Respir Physiol Neurobiol* **15**:9–22.
61. Silva JN, Oliveira LM, Souza FC, Moreira TS, Takakura AC (2019) Distinct pathways to the parafacial respiratory group to trigger active expiration in adult rats. *Am J Physiol Lung Cell Mol Physiol* **317**:L402–L413.
62. Schmitz C, Hof PR (2005) Design-based stereology in neuroscience. *Neuroscience* **130**:813–831.
63. Sparta DR, Stamatakis AM, Phillips JL, Hovelsø H, van Zessen R, Garret GD (2012) Construction of implantable optical fibers for long-term optogenetic manipulation of neural circuits. *Nat Protoc* **7**:12.
64. Takakura AC, Moreira TS, Colombari E, West GH, Stornetta RL, Guyenet PG (2006) Peripheral chemoreceptor inputs to retrotrapezoid nucleus (RTN) CO2-sensitive neurons in rats. *J Physiol* **572**(Pt2):503–523.
65. Takakura AC, Moreira TS, Stornetta RL, West GH, Gwilt JM, Guyenet PG (2008) Selective lesion of retrotrapezoid Phox2b-expressing neurons raises the apnoeic threshold in rats. *J Physiol* **586**(Pt 12):2975–2991.
66. Takakura AC, Barna BF, Cruz JC, Colombari E, Moreira TS (2014) Phox2b-expressing retrotrapezoid neurons and the integration of central and peripheral chemosensory control of breathing in conscious rats. *Exp Physiol* **99**:571–585.
67. Tuppy M, Barna BF, Alves-dos-Santos L, Britto LRG, Chiavegatto S, Moreira TS, Takakura AC (2015) Respiratory deficits in a rat model of Parkinson's disease. *Neuroscience* **297**:194–204.
68. von Bartheld CS, Bahney J, Herculano-Houzel S (2016) The search for true numbers of neurons and glial cells in the human brain: a review of 150 years of cell counting. *J Comp Neurol* **524**:3865–3895.
69. Wickham H (2016) ggplot2: Elegant Graphics for Data Analysis. Springer: New York.
70. Yao L, Zhou Q (2017) Enhancing NMDA receptor function: recent progress on allosteric modulators. *Neural Plast* **2017**:2875904.
71. Zesiewicz TA, Baker MJ, Wahba M, Hauser RA (2003) Autonomic nervous system dysfunction in Parkinson's disease. *Curr Treat Options Neurol* **5**: 149–160.
72. Zhang Y, Conti MA, Malide D, Dong F, Wang A, Shmist YA *et al* (2012) Mouse models of MYH9-related disease: mutations in nonmuscle myosin II-A. *Blood* **119**: 238–250.
73. Zhu Y, Das K, Wu J, Lee MH, Tan P (2014) RNH1 regulation of reactive oxygen species contributes to histone deacetylase inhibitor resistance in gastric cancer cells. *Oncogene* **33**:1527–1537.

SUPPORTING INFORMATION

Additional supporting information may be found in the online version of this article at the publisher's web site: